J. Fluid Mech. (2000), *vol.* 425, *pp.* 133–160. Printed in the United Kingdom

© 2000 Cambridge University Press

Finite-amplitude salt fingers in a vertically bounded layer

By TIMOUR RADKO AND MELVIN E. STERN

Department of Oceanography, Florida State University, Tallahassee, FL 32306-4320, USA

(Received 13 October 1999 and in revised form 26 June 2000)

We compute numerically the amplitude of long thin fingers that form in a liquid stratified with sugar S^* and salt T^* (measured in buoyancy units), for which $\tau = k_S/k_T = 1/3$ is the ratio of the two diffusivities and the Prandtl number is $Pr = \nu/k_T \sim 10^3$, where ν is the viscosity. The finger layer in our model is bounded by rigid and slippery horizontal surfaces with constant T^*, S^* (the setup is similar to the classical Rayleigh convection problem). The numerically computed steady fluxes compare well with laboratory experiments in which the fingers are sandwiched between two deep (convectively mixed) reservoirs with given concentration differences ΔT^*, ΔS^*. The model results, discussed in terms of a combination of asymptotic analysis and numerical simulations over a range of density ratio $R = \Delta T^*/\Delta S^*$, are consistent with the $(\Delta S^*)^{4/3}$ similarity law for the fluxes. The dimensional interfacial height (H^*) in the reservoir experiments (unlike that in our rigid lid model) is not an independent parameter, but it adjusts to a statistically steady value proportional to $(\Delta S^*)^{-1/3}$. This similarity law is also explained by our model when it is supplemented by a consideration of the stability of the very thin horizontal boundary layers with large gradients ($\partial S^*/\partial z$) which form near the rigid surfaces. The preference for three-dimensional salt fingers is also explained by a combination of analytical and numerical considerations.

1. Introduction

The laboratory setup that has most often been used to obtain the fluxes for doubly diffusive convection consists of two deep and well-mixed fluid reservoirs, between which long salt fingers form in some finite vertical interval $0 < z < H^*$ (e.g. Lambert & Demenkow 1971), where H^* is a dimensional height. Although double diffusion in the ocean (see the review of Schmitt 1994) involves salt and heat, with a small diffusivity ratio ($\tau = 1/80$), the experimental difficulties in realizing this are such that in most of the laboratory experiments an isothermal two-solute fluid (e.g. sugar and salt) is used to obtain physical insight into salt fingering. Accordingly the symbol S^* will subsequently refer to the density anomaly due to the substance (sugar) with lower diffusivity (k_S) and T^* will correspondingly refer to the density anomaly of the substance (salt) with higher diffusivity (k_T). (Thus the thermal and salinity expansion coefficients are absorbed in the concentrations.) In this case $\tau = 1/3$, $Pr = \nu/k_T \sim 10^3 \gg 1$ and a useful asymptotic expansion may be made (§ 2) in the Prandtl number Pr.

Laboratory experiments (e.g. Linden 1978) show that at the ends ($z = 0, H^*$) of the fingers there are very thin horizontal transition layers with large gradients ($\partial S^*/\partial z$, $\partial T^*/\partial z$), which couple the finger region to the reservoirs. The vertical velocity within

https://doi.org/10.1017/S0022112000002135 Published online by Cambridge University Press

an individual finger is greatly reduced as it approaches and passes the transition region. The fingers are then sheared as they pass through the transition layer and merge into buoyant plumes which maintain the large-scale convective turbulence in the reservoirs. Clearly, the connection conditions at $z = 0, H^*$ for the finger region are intractable, and one seeks a simpler model which can partially explain the laboratory observations. Radko & Stern (1999) suggested that the flux laws in the reservoir experiment could be understood (within a factor of two) using the parallel plate geometry of the classical Rayleigh convection problem, i.e. by assuming rigid slippery surfaces at $z = 0, H^*$, across which specified $\Delta T^*, \Delta S^*$ are maintained. In this paper such calculations are made over a wide range of density ratios $R = \Delta T^*/\Delta S^*$ and H^*; the magnitudes and ratio of the two fluxes are compared with the experiment.

An obvious difference between our model and the laboratory experiments is that H^* in the former case is an independent variable, whereas the experimental H^* adjusts from its initial height to a unique value depending on $(\Delta T^*, \Delta S^*)$, as was convincingly verified by Linden (1978). Stern & Turner (1969) suggested that the fluxes in the quasi-equilibrium state are also independent of the initial value of the interfacial height and are functions of $\Delta T^*, \Delta S^*$ only. The consequent dimensional arguments results in the similarity law (first suggested by Turner 1967) for the fluxes:

$$F_S = C(R, \tau, \nu/k_T)(\Delta S^*)^{4/3}.$$

The value of the flux law constant C measured by Stern & Turner (1969) is $C \sim 10^{-2}\,\mathrm{cm\,s^{-1}}$, while Lambert & Demenkow (1971) found values of C ranging from 0.5×10^{-3} to 0.75×10^{-3}. These results were partially reconciled by Griffiths & Ruddick (1980) who measured C for various density ratios, and discovered that the dependence of C on R is extremely strong: approximately $C \sim R^{-6}$. Taylor & Veronis (1996) concentrated on large values of density ratios $2.5 < R < 3$ (corresponding to a weak instability) and also observed the $C \sim R^{-6}$ dependence, even though their values were offset from the previous results (Griffiths & Ruddick 1980) towards larger values of C. A theoretical explanation of such a rapid decrease in the fluxes with R will be given in § 5, and it will be shown that the values of C computed from our model are consistent with the experiments for various values of H^*. Such an agreement implies that the dependence of C on H^* in the rigid lid model is very weak, a result which is also explained in § 5.

A separate question is how to explain the (unique) H^* in the experiments. Shen (1989) used direct numerical simulations to study the formation of salt finger layers and suggested that the breakup of fingers occurs due to the processes in the thin boundary layers (with local density inversions) at the edges of the finger interface. This idea is developed further (§ 6) in the present paper in order to obtain an explicit expression for the equilibrium H^*.

One of the most interesting aspects of salt fingering is the statistics of their horizontal pattern selection. In the linear instability theory the growth rate of a normal mode with large vertical wavelength is determined only by the absolute value of the horizontal wavenumber, and therefore, according to the linear theory, any planform of motion satisfying the Helmholtz equation with the same wavenumber is equally likely to be realized (wavenumber degeneracy). However, the observations of finite-amplitude salt fingers (e.g. Shirtcliffe & Turner 1970) indicate that they have a remarkably regular square cross-section. This preference must be due to the nonlinear interactions between different modes (or to statistical considerations). Proctor & Holyer (1986) attempted to explain the planform selection by developing a weakly nonlinear theory for the long thin salt fingers. However, they concluded,

https://doi.org/10.1017/S0022112000002135 Published online by Cambridge University Press

in conflict with the experiments, that the (two-dimensional) roll-type planforms are preferred over the square cells. One reason for the disagreement might be that their expansion was pivoted about a mode of zero growth rate (unlike the present paper where the expansion includes the fastest growing modes). Another and probably more important reason is that thin horizontal boundary layers form at the edges of the finger zone and these have not been properly represented in the Proctor & Holyer's theory. We show that these boundary layers are extremely important for the planform selection, and prove that when these layers are included the rolls are unstable with respect to 'cross-roll' perturbations. In some cases this instability leads to a disruption of the rolls and formation of the square cells, which may explain the observed three-dimensional structure of the salt fingers.

The reservoir experiments discussed above should be distinguished from the less frequent (but more oceanically relevant) setup consisting of an effectively unbounded finger domain, whose undisturbed state consists of uniform vertical gradients $\partial \bar{T}^*/\partial z$, $\partial \bar{S}^*/\partial z$ (Stern & Turner 1969; Taylor 1993). In that case the evolved statistically steady fluxes depend on these temperature and salinity gradients, rather than on the temperature–salinity differences $(\Delta T^*, \Delta S^*)$ as in the present reservoir experiments. An unbounded model was considered by RS, who computed the fluxes for a limited range of the density ratios, assuming the three-dimensional spatial periodicity of the temperature and salinity perturbations.

2. Preliminary calculations

Our starting point is the Boussinesq equations which are non-dimensionalized using the conventional 'salt finger width' $\lambda = (k_T \nu / g \bar{T}_z^*)^{1/4}$ as the dimensional length scale, where $\bar{T}_z^* = \Delta T^*/H^*$ is the undisturbed dimensional temperature gradient (recall that ΔT^* is the temperature difference across the finger layer in buoyancy units and H^* is the dimensional height). $T_z^* \lambda$ is used as the scale for both salinity and temperature perturbations, k_T/λ is the velocity scale, and $\nu k_T/\lambda^2$ is the pressure scale. Let $[T(x, y, z, t), S(x, y, z, t)]$ denote the non-dimensionalized departures of the temperature and salinity from the undisturbed (linear) state $[\bar{T}(z), \bar{S}(z)]$; $[\theta(z), \sigma(z)]$ are the horizontal averages of (T, S) and $T' \equiv T - \theta(z, t), S' \equiv S - \sigma(z, t)$.

When the assumption $Pr = \nu/k_T \gg 1$, appropriate to sugar–salt fingers ($Pr \sim 800$), is made the Boussinesq equations reduce to the high Prandtl number equations

$$0 = -\nabla p + \nabla^2 \boldsymbol{v} + (T' - S')\boldsymbol{k}, \tag{2.1a}$$

$$\nabla \cdot \boldsymbol{v} = 0, \tag{2.1b}$$

$$\frac{\mathrm{d}}{\mathrm{d}t} T + w = \nabla^2 T, \tag{2.1c}$$

$$\frac{\mathrm{d}}{\mathrm{d}t} S + (1/R) w = \tau \nabla^2 S. \tag{2.1d}$$

The influence of the undisturbed $\bar{T}(z), \bar{S}(z)$ fields appears in the coefficients of w. The rigid boundaries are at $z = 0$, $z = H$, where $T = S = w = 0$ and H is a non-dimensional height of the finger zone. In addition to the calculations made using (2.1), which will be discussed below, we also made several numerical experiments (not shown) with the full Navier–Stokes system of equations for large but finite values of Pr and verified that the results for $Pr > 10$ differ little from those obtained using the much simpler asymptotic system (2.1).

https://doi.org/10.1017/S0022112000002135 Published online by Cambridge University Press

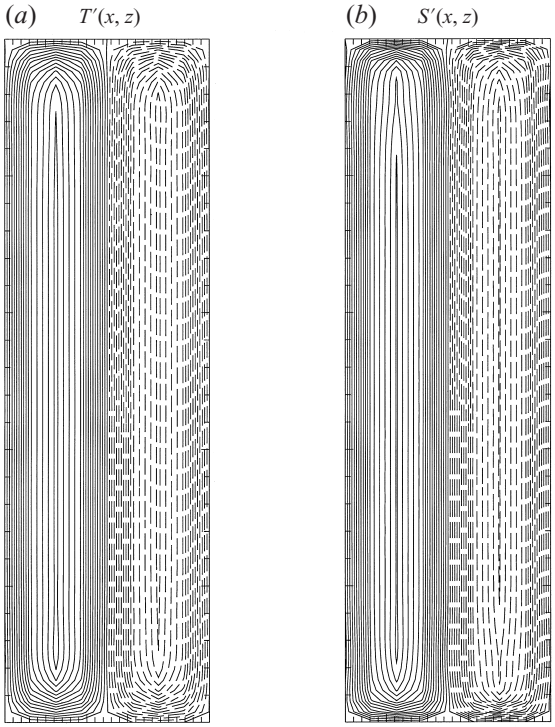


FIGURE 1. (*a*) T' isopleths for the steady two-dimensional fingers obtained by the numerical integration of (2.1) for $R = 2.6$. (*b*) S' isopleths for the state in (*a*). Calculations were initiated by a normal mode (for the undisturbed state) with aspect ratio 1 : 10. Note the remarkably uniform region in the interior of the domain and the boundary layers near $z = 0, H$ whose thickness is comparable to the finger width.

We solved equations (2.1) numerically using a fully dealiased pseudo-spectral method in which all the equations were inverted exactly in the Fourier space. The linear diffusive terms were evaluated using the integrating factors technique (Canuto *et al.* 1987), and a fourth-order Runge–Kutta scheme was used for the time integration. This code was described in RS, and in the present rigid boundary problem we only modified it by using a Fourier expansion of (T, S, w) in $\sin(mz)$ functions, rather than the $\exp(imz)$ set employed in the unbounded model (RS). In all the following calculations we keep $\tau = 1/3$ (corresponding to the sugar–salt laboratory experiment) and consider various values of the aspect ratio $\mu =$ (fastest growing wavelength)/$(2H)$ and of the density ratio $R = \bar{T}_z/\bar{S}_z$.

We start with a strictly two-dimensional numerical calculation with the aspect ratio $\mu = 0.1$, initialized with the fastest growing linear normal mode (Stern & Radko 1998) hereafter) using the relatively large (i.e. close to τ^{-1}) $R = 2.6$:

$$T = 0.2 \sin(k_f x) \sin(mz), \quad \text{where} \quad k_f \approx \left(\frac{\varepsilon}{3}\right)^{1/4}, \ \varepsilon = \frac{1}{R\tau} - 1. \tag{2.2}$$

Although this value of k corresponds to the maximum growth rate for the long waves ($m/k_f \to 0$) and for small ε (Stern & Radko 1998), it is close to that for the small but finite values of m and ε used herein. Even for large ε the exact value of the fastest growing wavelength does not differ much from that corresponding to (2.2); in particular, for $R = 1.4$ (which is one of the smallest values of density

https://doi.org/10.1017/S0022112000002135 Published online by Cambridge University Press

ratio considered herein) the exact fastest growing wavelength is $L = 10.66$, while (2.2) gives $L = 7.99$, and the corresponding fluxes are also comparable. The computational grid for this calculation, consisting of $(N_x, N_z) = (8, 64)$ points, resolved only one finger pair, and the time step employed was $\Delta t = 0.1$. Initially this disturbance was growing exponentially in agreement with the linear theory, but by $t = 1000$ its growth was nonlinearly stabilized as the (T, S^*) field evolved to the steady state in figure 1(a, b). Note the remarkably uniform (in z) structure of fingers in the interior and the well-defined purely diffusive boundary layers at $z = 0, H$. The vertical thickness (d) of these is comparable to the finger width for the state in figure 1, but the detailed examination of the boundary layers in § 5 will reveal a weak dependence of d on the aspect ratio μ. Such structures have been observed in most of our experiments for long ($m/k_f \ll 1$) fingers, and some other examples of these steady states also appear in Stern & Radko (1998) and Radko & Stern (1999). (Paparella & Spiegel 1999 obtained highly truncated solutions that look similar to ours, although their Prandtl and Lewis numbers are much different from those for salt–sugar.)

A similar three-dimensional solution was obtained by initiating the calculation using a 'square cell' normal mode with the same $(\mu, R) = (0.1, 2.6)$

$$T = 0.2(\sin(k_f x) + \sin(k_f y))\sin(mz).$$

This calculation also resulted in a steady state (not shown) with a remarkably uniform interior and diffusive boundary layers at $z = 0, H$. The horizontal planform remained square, even when the steady state was reached. Especially noteworthy is the fact that the integral characteristics for this square cell solution were close to those for the two-dimensional counterpart; in the two-dimensional case the non-dimensional heat flux (Nusselt number based on the purely convective flux and the undisturbed $\bar{T}_z$) was $Nu \equiv \langle \overline{wT} \rangle = -0.25$, while in the three-dimensional case $Nu = -0.24$. (Hereafter the angular brackets $\langle \ldots \rangle$ will denote the vertical average and overbar is a horizontal average; the combination of the two is a volume average). The fact that in a rigid lid model the two-dimensional fluxes are close to the corresponding three-dimensional ones will be explained in a following asymptotic mean field theory (§ 3).

In order to demonstrate the representativeness of the calculation with only one finger pair (in which periodicity was assumed on the distances corresponding to the fastest growing horizontal wavelength) as compared to multiple fingers, we made calculations for much larger horizontal sizes of the computational domain. Figure 2 shows the three-dimensional fingers that occur when the size of computational domain (in both x and y) exceeds the finger wavelength ($2\pi/k_f$) by a factor of 5. This calculation for $R = 2.6$ was initiated by a small random initial perturbation and did not result in the completely steady state; instead the spatially averaged fluxes oscillate around the statistical averages. For future comparison of our 'rigid lid' model with the observations we indicate that the flux ratio (ratio of the flux of temperature to the flux of salt) for the calculation in figure 2 is $\gamma = 0.95$. Despite the apparent differences in the vertical cross-sections of fingers in figure 1 and figure 2 (both for $\mu = 1:10$, $R = 2.6$), the fluxes in these states are quite comparable: in the former case we have $Nu = -0.247$ and in the latter $Nu = -0.27$. The fluxes in the multiple-finger runs are given in table 1 for fixed $\mu = 1:10$, and for a wide range of density ratios. When these multiple-finger fluxes were compared with fluxes in the corresponding single-finger-pair calculations (either two- or three-dimensional calculations, since these are close) we discovered that the difference between the two is small for large values of R but many reach $\sim 50\%$ level for low R.

Another test of sensitivity to the changes in size of the computational domain

https://doi.org/10.1017/S0022112000002135 Published online by Cambridge University Press

R	$-\langle\overline{wT'}\rangle$ 3D (5×5 finger pairs)
2.6	0.27
2.4	0.49
2.2	0.78
2.0	1.07
1.8	1.48
1.6	1.96
1.4	2.50

TABLE 1. Heat flux (Nu) as a function of R for the large horizontal sizes ($10\pi(\varepsilon/3)^{-0.25}$) of the computational box. Aspect ratio is $\mu = 1:10$. All the runs were initiated by a small three-dimensional random perturbation.

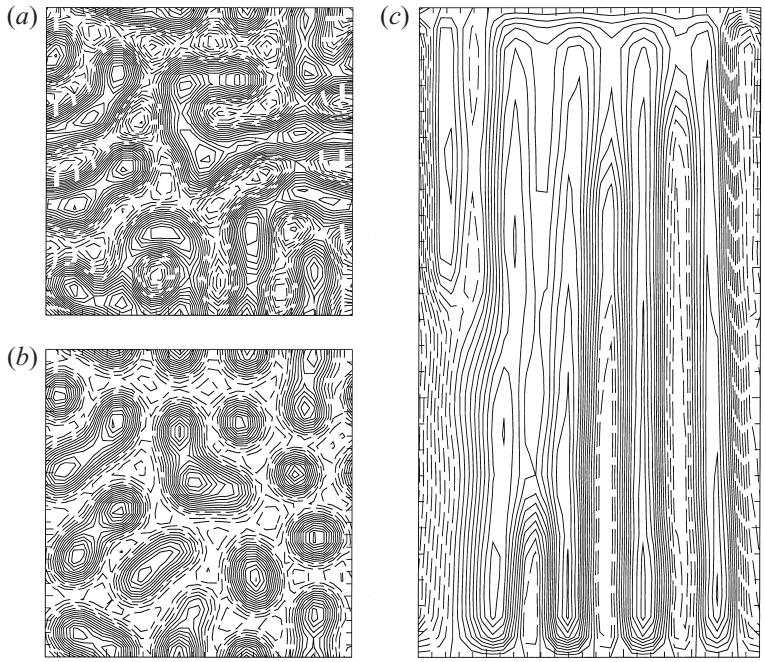


FIGURE 2. The isotherms of the three-dimensional state at the end of calculation ($t = 1600$) with large computational domain (approximately 5×5 fastest growing wavelengths) and $R = 2.6$. The height of the computational domain is ten times larger than the fingerwidth. (*a*) Horizontal cross-section across the interior of the finger zone at $z = H/2$; (*b*) horizontal cross-section across the boundary layer ($z = H/32$); (*c*) vertical cross-section along the $y = 0$ plane.

was made using a three-dimensional calculation (not shown) in which the distance between the x and y boundaries was equal to 3 fastest growing wavelengths (instead of 5 wavelengths in table 1). This calculation for $R = 1.4$ was performed using a $(32, 32, 64)$ grid (i.e. about 10 points per fingerwidth) and resulted in $Nu = -2.5$, which is consistent with the value for the corresponding five-finger calculation in table 1. In order to make sure that the resolution used in this work (typically ~ 8 points per finger pair) is sufficient for a reliable estimate of fluxes in the rigid lid model we reproduced the foregoing experiment using much worse resolution (5 points per finger pair). The resulting equilibrium fluxes changed by less than 1% and the

https://doi.org/10.1017/S0022112000002135 Published online by Cambridge University Press

structure of the (T, S) fields was quite similar to that obtained previously, which proves the adequacy of the resolution. The fact that the fluxes are comparable in the experiments with different horizontal sizes of the computational domain implies that the long finite horizontal wavelengths (not included in the one-finger-pair calculations) are not of major physical importance for the nonlinear equilibration. Thus, in order to explain the mechanism of stabilization we may consider a very simple steady-state one-finger-pair model in which the horizontal periodicity corresponds to the fastest growing wavelength (2.2).

3. Asymptotic formulations ($\varepsilon \to 0$)

3.1. *Two-dimensional theory*

Consider first a simple case of a two-dimensional motion $(T, S) = [T(x, z), S(x, z)]$. The linear theory (see Stern & Radko 1998) suggests using the (space, time) scales $(\varepsilon^{-1/4}, \varepsilon^{-3/2})$ of the fastest growing mode to transform (2.1), i.e. the new coordinates x_0, z_0, t_0 are given by

$$x = \varepsilon^{-1/4} x_0, \quad z = \varepsilon^{-1/4} z_0, \quad t = \varepsilon^{-3/2} t_0.$$

(As we shall see this rescaling does not preclude a slower z variation in the fingers outside the $z = 0, H$ boundary layers.)

Let us assume that the (ε) scale of the temperature is ε^q, where the exponent q is yet to be determined. The leading-order $(\varepsilon^{q+1/2})$ balances of the linear terms in the advection diffusion equations (2.1c, d) suggest scaling of the vertical velocity as $w \sim \varepsilon^{1/2} T \sim \varepsilon^{q+1/2}$ and the salinity $S \sim T$ as ε^q. Next, we consider the perturbations which are (at the leading order) harmonic functions of x with a horizontal wavelength corresponding to the fastest growing mode:

$$T = \varepsilon^q T_0 \sin k_0 x_0 + \cdots, \quad S = \varepsilon^q S_0 \sin k_0 x_0 + \cdots, \quad w = \varepsilon^{q+1/2} w_0 \sin k_0 x_0 + \cdots, \quad (3.1a)$$

where $k_0^4 = (1/3)^{0.25}$ is a rescaled fastest growing wavenumber: the following theory will show that this structure of the expansion is retained in the temporal evolution. When (3.1a) is substituted in (2.1c, d) and the limit $\varepsilon \to 0$ is taken the result is

$$w_0 = \left(\frac{\partial^2}{\partial z_0^2} - k_0^2 \right) T_0, \quad S_0 = T_0, \qquad (3.1b)$$

and the continuity equation is satisfied if

$$u = \varepsilon^{q+1/2} u_0 \cos k_0 x_0, \quad u_0 = \left(k_0^{-1} \frac{\partial^3}{\partial z_0^3} - k_0 \frac{\partial}{\partial z_0} \right) T_0.$$

The nonlinear terms $\nabla \cdot (\boldsymbol{v} T), \nabla \cdot (\boldsymbol{v} S)$ in equations (2.1c, d) eventually equilibrate the linear growth of the perturbation. At the leading order these terms result in generation of the two new modes, one of which corresponds to a mean field modification $[\theta(z, t), \sigma(z, t)]$, and the other mode $(2k_f)$ corresponds to the non-resonant triad (or wave–wave) interaction. Although modes of both types formally appear at the same order $(\varepsilon^{2q+1/4})$, we shall now show that the $k = 2k_f$ term is much smaller in amplitude than the mean-field term (θ, σ). In figure 1, for example, the variance in $\theta(z, t)$ was 7.1×10^{-2}, while only 1.1×10^{-5} was in mode $k = 2k_f$. To explain such a difference in amplitudes of these terms consider the leading-order $(\varepsilon^{2q+3/4})$ balance of the

https://doi.org/10.1017/S0022112000002135 Published online by Cambridge University Press

horizontally averaged advection diffusion equations. In the rescaled variables this is

$$\left.\begin{aligned}\frac{1}{2}\frac{\partial}{\partial z_0}\left[\left(\frac{\partial^2}{\partial z_0^2}-k_0^2\right)T_0\cdot T_0\right]&=\frac{\partial^2}{\partial z_0^2}\theta_0,\\ \frac{1}{2}\frac{\partial}{\partial z_0}\left[\left(\frac{\partial^2}{\partial z_0^2}-k_0^2\right)T_0\cdot T_0\right]&=\tau\frac{\partial^2}{\partial z_0^2}\sigma_0,\end{aligned}\right\}\tag{3.2a}$$

where $(\theta,\sigma)=\varepsilon^{2q+1/4}(\theta_0,\sigma_0)$. For the $(2k_f)$ mode $\varepsilon^{2q+1/4}(T_{tr},S_{tr})\cos(2k_0x_0)$ the corresponding leading order balance is

$$\left.\begin{aligned}\frac{1}{2}\left[\frac{\partial^3}{\partial z_0^3}T_0\cdot T_0-\frac{\partial^2}{\partial z_0^2}T_0\cdot\frac{\partial}{\partial z_0}T_0\right]&=\left(\frac{\partial^2}{\partial z_0^2}-4k_0^2\right)T_{tr},\\ \frac{1}{2}\left[\frac{\partial^3}{\partial z_0^3}T_0\cdot T_0-\frac{\partial^2}{\partial z_0^2}T_0\cdot\frac{\partial}{\partial z_0}T_0\right]&=\tau\left(\frac{\partial^2}{\partial z_0^2}-4k_0^2\right)S_{tr}.\end{aligned}\right\}\tag{3.2b}$$

The numerical calculations in the previous section indicate that the variation of the (T,S) field in the interior, i.e. outside the thin boundary layers near $z=0,H$, occurs on a large vertical scale (see the almost uniform interior region in figure 1a,b). Thus in the interior $\partial/\partial z_0\sim H_0^{-1}\sim\mu k_0\ll k_0$, and therefore (3.2$a,b$) yields $\theta_0\sim k_0^2\mu^{-1}T_0^2$, $T_{tr}\sim\mu^3k_0^{-2}T_0^2$, or $T_{tr}/\theta_0\sim\mu^4\ll1$ for $\mu\ll1$. At the lower (say) boundary layer the continuity of temperature across its upper edge ($z_0=d_0$) implies that $\partial T_{tr}/\partial z_0\sim(1/d_0)T_{tr}|_{z_0=d_0}$ is also small $[O(\mu^{-4})]$ compared to $\partial\theta_0/\partial z_0\sim(1/d_0)\theta_0|_{z_0=d_0}$; likewise for the upper boundary layer. Thus, the nonlinear terms resulting from the mean field–fundamental harmonic interaction (e.g. $w_0\partial\theta_0/\partial z_0$) will exceed the corresponding triad terms (such as $w_0\partial T_{tr}/\partial z_0\sim u_0\partial T_{tr}/\partial x_0$) by a large factor of $O(\mu^{-4})$ in the boundary layers as well as in the interior. Another reason for neglecting the 'triad' or wave–wave interaction terms (one which is more relevant for the short fingers with $\mu=O(1)$) is that in the spectral decomposition of T^* the dominant mode in z is a fundamental one proportional to $\sin m_0z_0$ (see figure 1), and for such a (two-dimensional) mode the left-hand side of (3.2b) vanished identically, while the left-hand side of (3.2a) is finite. This implies that the amplitude of T_{tr},S_{tr} is much less than the amplitude of θ_0,σ_0. These considerations lead us to the following nonlinear mean field theory, similar to that in the classical Rayleigh convection problem (Malkus & Veronis 1958). In the later case, however, the cell aspect ratio is $O(1)$, whereas in our theory μ is small, and this justifies the following neglect of the triad terms (T_{tr},S_{tr}) in two (and three) dimensions.

The nonlinear interaction of the mean fields $(\theta,\sigma)=\varepsilon^{2q+1/4}(\theta_0,\sigma_0)$ with the leading-order k_0 mode will result in the generation of the higher order $\sin k_0x_0$ terms, and their scale is obtained from a balance between the nonlinear (e.g. $w\,\partial\theta/\partial z\sim\varepsilon^{3q+1}$) and the diffusive terms:

$$\left.\begin{aligned}T&=\varepsilon^qT_0\sin k_0x_0+\varepsilon^{2q+1/4}\theta_0+\varepsilon^{3q+1/2}T_2\sin k_0x_0\ldots,\\ S&=\varepsilon^qT_0\sin k_0x_0+\varepsilon^{2q+1/4}\sigma_0+\varepsilon^{3q+1/2}S_2\sin k_0x_0\ldots\ .\end{aligned}\right\}\tag{3.3}$$

At all orders we have to satisfy the vorticity equation (obtained from (2.1a,b))

$$\nabla^4w=\frac{\partial^2}{\partial x^2}(S-T),\tag{3.4}$$

and when (3.3) is substituted in (3.4) it becomes apparent that the vertical velocity should be expanded as

$$w=\varepsilon^{q+1/2}w_0\sin k_0x_0+\varepsilon^{3q+1}w_2\sin k_0x_0\ldots\ .$$

Since $(\partial/\partial t)(T,S)\sim\varepsilon^{3/2}\varepsilon^q$ is required to be of the same order as the nonlinear $\sin k_0x_0$

https://doi.org/10.1017/S0022112000002135 Published online by Cambridge University Press

terms (e.g. $w\,\partial\theta/\partial z \sim \varepsilon^{3q+1}$) it follows that

$$q = \tfrac{1}{4}. \tag{3.5}$$

For future use we note

$$\frac{\partial}{\partial z}(\theta, \sigma) = \varepsilon \frac{\partial}{\partial z_0}(\theta_0, \sigma_0). \tag{3.6}$$

The order $\varepsilon^{3q+1} = \varepsilon^{7/4}$ balance of the advection–diffusion equations (2.1c, d), using $1/R = \tau(1+\varepsilon)$, then gives the *prognostic* equations:

$$\left.\begin{aligned} \frac{\partial}{\partial t_0} T_0 + w_0 \frac{\partial}{\partial z_0}\theta_0 + w_2 &= \left(\frac{\partial^2}{\partial z_0^2} - k_0^2\right) T_2, \\ \frac{\partial}{\partial t_0} T_0 + w_0 \frac{\partial}{\partial z_0}\sigma_0 + \tau w_0 + \tau w_2 &= \tau\left(\frac{\partial^2}{\partial z_0^2} - k_0^2\right) S_2. \end{aligned}\right\} \tag{3.7}$$

The leading-order ($\varepsilon^{3/2}$) balance of the equation (3.4) gives

$$\left(\frac{\partial^2}{\partial z_0^2} - k_0^2\right)^3 T_0 = k_0^2 (T_2 - S_2), \tag{3.8}$$

where (3.1b) was used to eliminate w_0. By eliminating w_2 in (3.7) and then using (3.8) to eliminate $(T_2 - S_2)$ we obtain

$$(1-\tau)\frac{\partial}{\partial t_0} T_0 + w_0 \frac{\partial}{\partial z_0}(\sigma_0 - \tau\theta_0) + \tau w_0 = -k_0^{-2}\tau \left(\frac{\partial^2}{\partial z_0^2} - k_0^2\right)^4 T_0. \tag{3.9}$$

Finally, (3.2a) is used to eliminate $(\partial/\partial z_0)(\sigma_0, \theta_0)$ and (3.1b) is used to eliminate w_0. Then (3.9) reduces to a single evolution equation for T_0:

$$\begin{aligned} (1-\tau)\frac{\partial}{\partial t_0} T_0 + \frac{1}{2}\left(\frac{1}{\tau} - \tau\right)\left(\frac{\partial^2}{\partial z_0^2} - k_0^2\right) T_0 \left[\left(\frac{\partial^2}{\partial z_0^2} - k_0^2\right) T_0 \cdot T_0 \right. \\ \left. - \left\langle \left(\frac{\partial^2}{\partial z_0^2} - k_0^2\right) T_0 \cdot T_0 \right\rangle\right] + \tau\left(\frac{\partial^2}{\partial z_0^2} - k_0^2\right) T_0 + k_0^{-2}\tau \left(\frac{\partial^2}{\partial z_0^2} - k_0^2\right)^4 T_0 = 0. \end{aligned} \tag{3.10}$$

It is important to note that although $\partial/\partial z_0$ in (3.10) may be small (for $\mu \to 0$) compared to k_0 in the interior, this equation also describes the boundary layers where $\partial/\partial z_0$ is large and cannot be neglected.

Equation (3.10) for a single field variable is much simpler than the original system (2.1), and the numerical integration of (3.10) is also extremely fast. When (3.10) was solved numerically for the aspect ratio $\mu = 1:10$ using a small initial perturbation consisting of a normal mode ($T_0 = 0.2 \sin m_0 z_0, m_0 = \mu k_0$), the integration resulted in a steady state (figure 3a, b). This asymptotic solution again reveals the remarkably uniform interior of the fingers as well as the boundary layers near $z = 0, H$, features which have been observed in the solutions of the fully nonlinear equations (2.1) (see figure 1).

The foregoing asymptotic theory leads to the following scalings of heat flux, r.m.s. temperature and density flux

$$\langle \overline{wT} \rangle \sim \varepsilon, \quad \langle \overline{T'^2} \rangle^{1/2} \sim \varepsilon^{1/4}, \quad \langle \overline{w(T' - S')} \rangle \sim \varepsilon^2.$$

(We remark in passing that these rigid lid results differ significantly from the asymptotic theory for an *unbounded* model (see Radko & Stern 1999)). The rescaled heat flux (Nusselt number) for the calculation $\mu = 0.1$ in figure 3(a, b) is $Nu_0 = \varepsilon^{-1} Nu = -1.67$, and the rescaled r.m.s. temperature variation is $\langle 0.5 T_0^2 \rangle^{1/2} = 1.67$.

https://doi.org/10.1017/S0022112000002135 Published online by Cambridge University Press

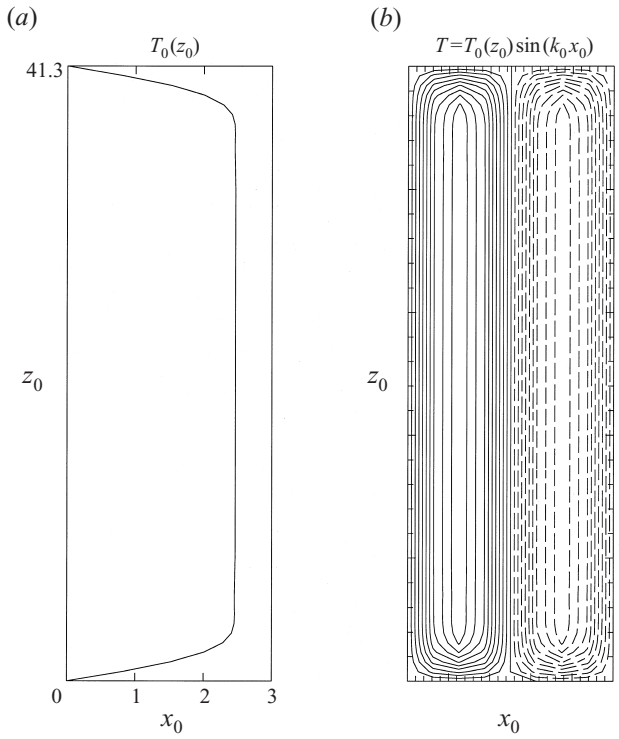


FIGURE 3. (*a*) The steady solution of (3.10) $T_0(z_0)$ for the aspect ratio of $\mu = 1:10$. (*b*) The rescaled isopleths of the leading-order temperature field $T_0(z_0)\sin k_0x_0$ (also for $\mu = 1:10$). Note the boundary layers at the top and at the bottom, of thickness comparable to the finger width; note also the remarkably uniform interior. This figure should be compared with the corresponding solution of the original equations in figure 1. The rescaled Nusselt number for this state is $Nu_0 = \varepsilon^{-1}Nu = -1.67$.

In order to estimate the accuracy of the $\varepsilon \to 0$ theory we performed finite-ε numerical calculations with one fully resolved finger pair using the original system (2.1). We found steady states (similar to that in figure 1) for $1.2 < R < 2.9$ and fixed $\mu = 1:10$. The results are in table 2, which demonstrate that the region of validity of (3.10) significantly exceeds that required by $\varepsilon = [(\tau R)^{-1} - 1] \ll 1$, and provides an additional justification for the neglect of the triad terms (at least for $\mu = 0.1$ employed here). Even for the largest value of ε considered, corresponding to $R = 1.2$, the error in $\varepsilon \to 0$ theory (for the temperature amplitude) is only 30%; and for the typical value of density ratio $R \sim 1.6$ for the laboratory sugar–salt experiments (Lambert & Demenkow 1971) the error is $\sim 17\%$. We also note that although formal analysis allows us to neglect the triad terms ($k = 2k_0$) only for long fingers ($\mu \ll 1$), additional numerical calculations (not shown) indicate that this mean field theory is quite accurate for all values of μ, not only the small ones.

It now only remains to determine how our asymptotic solution depends on the aspect ratio (μ). For this purpose we numerically obtained the steady solutions of (3.10) for $\mu = 1:10, 1:20, \ldots, 1:160$. All the solutions look similar to that in figure 3(*a*, *b*), and the rescaled fluxes (Nu_0) for these steady states are plotted as a function of μ (using logarithmic coordinates) in figure 4. All the points in figure 4 fall on an almost straight line whose slope corresponds to a power law $Nu_0(\mu) \propto \mu^{-1.2}$. This relationship will be explained by considering the $\mu \to 0$ limit (§ 5).

https://doi.org/10.1017/S0022112000002135 Published online by Cambridge University Press

R	$Nu = -\langle\overline{wT}\rangle$ using (2.1)	$-\varepsilon Nu_0$	$\langle\overline{T^2}\rangle^{1/2}$ using (2.1)	$\langle 0.5T_0^2\rangle^{1/2}\varepsilon^{1/4}$	Relative error in r.m.s. T' (%)
2.9	0.0566	0.0575	0.71	0.72	1
2.8	0.117	0.119	0.85	0.86	1
2.6	0.247	0.256	1.02	1.04	2
2.4	0.385	0.417	1.12	1.18	5
2.2	0.547	0.607	1.21	1.29	7
2.0	0.725	0.835	1.28	1.40	9
1.8	0.920	1.113	1.34	1.51	13
1.6	1.137	1.461	1.38	1.61	17
1.4	1.379	1.908	1.41	1.72	22
1.2	1.651	2.505	1.42	1.84	30

TABLE 2. Comparison of the asymptotic theory with the exact one-finger-pair calculation.

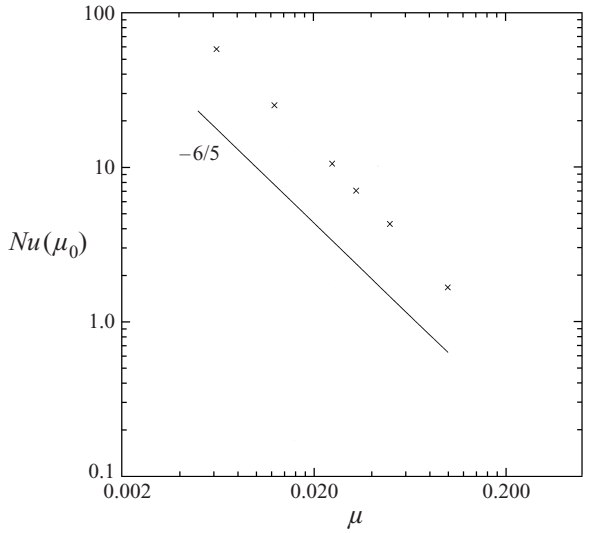


FIGURE 4. The rescaled Nusselt number as a function of the aspect ratio μ in logarithmic coordinates. All the data points $Nu_0(\mu)$ (denoted by crosses) belong to a straight line whose slope corresponds to a power law $Nu_0 \propto \mu^{-1.2}$.

3.2. *Three-dimensional case*

Let us use the scalings determined in the foregoing two-dimensional calculations for a three-dimensional asymptotic theory starting with

$$T = \varepsilon^{1/4} T_1(z_0) \sin k_0 x_0 + \varepsilon^{1/4} T_2(z_0) \sin k_0 y_0 + (\text{higher-order terms}). \tag{3.11}$$

The nonlinear advection terms in (2.1c, d) will now result in the generation of the four types of modes at the order $\varepsilon^{3/4}$; these include the mean-field mode (θ, σ) and the modes proportional to $\cos 2k_0 x_0$, $\cos 2k_0 y_0$, $\sin k_0 x_0 \sin k_0 y_0$.

As was the case in the two-dimensional calculation we again find that among these modes the mean-field (θ, σ) terms are the largest. For example, in the square-cell steady state with $\mu = 1:10, R = 2.6$ (discussed in § 2), the temperature variance is distributed as follows: 5.88×10^{-2} is in the mean field θ, 6.6×10^{-3} is in the $\sin k_0 x_0 \sin k_0 y_0$ mode, and 6.5×10^{-6} is in each of the $2k_0$ modes. The relatively large

https://doi.org/10.1017/S0022112000002135 Published online by Cambridge University Press

amplitude of the mean-field terms can be rationalized in the same way as was done for the two-dimensional case: consideration of the asymptotic limit $\mu \to 0$ shows that the amplitude of the mean field should exceed the amplitudes of the $2k_0$ harmonics by a factor of $O(\mu^{-4}) \gg 1$, and exceed the $\sin k_0 x_0 \sin k_0 y_0$ mode by a factor $O(\mu^{-2}) \gg 1$.

It is easy to see that when the (small) triad terms are neglected, the three-dimensional equivalent of (3.10) is

$$(1-\tau)\frac{\partial}{\partial t_0}\begin{pmatrix} T_1 \\ T_2 \end{pmatrix} + \frac{1}{2}\left(\frac{1}{\tau}-\tau\right)\left(\frac{\partial^2}{\partial z_0^2}-k_0^2\right)\begin{pmatrix} T_1 \\ T_2 \end{pmatrix} \sum_{i=1,2}\left[\left(\frac{\partial^2}{\partial z_0^2}-k_0^2\right) T_i \cdot T_i \right.$$
$$\left. -\left\langle \left(\frac{\partial^2}{\partial z_0^2}-k_0^2\right) T_i \cdot T_i \right\rangle\right] + \tau\left(\frac{\partial^2}{\partial z_0^2}-k_0^2\right)\begin{pmatrix} T_1 \\ T_2 \end{pmatrix} + k_0^{-2}\tau\left(\frac{\partial^2}{\partial z_0^2}-k_0^2\right)^4\begin{pmatrix} T_1 \\ T_2 \end{pmatrix} = 0. \tag{3.12}$$

This system is totally degenerate with respect to the rolls vs. cells, in the following sense. If $T_0(z_0, t_0)$ is a solution of (3.10), then for all (α, β) such that $\alpha^2 + \beta^2 = 1$,

$$\begin{pmatrix} T_1 \\ T_2 \end{pmatrix} = \begin{pmatrix} \alpha T_0 \\ \beta T_0 \end{pmatrix} \tag{3.13}$$

will be a solution of (3.12). Thus, in this $\varepsilon \to 0$ mean-field theory all the possible planforms are equivalent, a feature which also occurs in the other weakly nonlinear asymptotic theories based only on the mean-field modification (see the mean-field theories cited by Proctor & Holyer 1986). It also follows from (3.12) that the integral characteristics of the two-dimensional solutions (fluxes, etc.) should be close to the corresponding three-dimensional solutions, which was indeed observed in our numerical calculations (see § 2).

Even though the foregoing mean-field theory (3.12) is very useful in estimating the amplitude of the fluxes and in explaining why the three-dimensional fluxes and structures are so close to those observed in two dimensions, any attempt to understand the planform selection must consider the evolution of the small $\sin k_0 x_0 \sin k_0 y_0$ mode that actually determines the planform (Proctor & Holyer 1986). Such an analysis will be presented in the following section, but the reader who is more interested in the relevance of the foregoing solutions to previous laboratory experiments may proceed directly to § 5.

4. Planform selection

4.1. *Instability of the steady two-dimensional rolls in the limit* $\varepsilon \to 0$

Consider a steady-state roll (3.1) oriented in the y-direction, whose temperature field at the leading order (according to the two-dimensional asymptotic theory in § 3.1) is

$$T_{basic} = \varepsilon^{1/4} T_1(z_0) \sin k_0 x_0, \tag{4.1}$$

where $T_1(z_0)$ is a steady-state solution of (3.10), such as presented in figure 3(a). Now introduce a relatively small perturbation consisting of a 'cross-roll' mode

$$T_{c-r} = \varepsilon^{\nu} \tilde{T}_2 \sin k_0 y_0 + \cdots, \tag{4.2}$$

and the 'interaction' mode (mostly responsible for the transfer of energy from the basic state (4.1) to the 'cross-roll' mode (4.2))

$$T_{int} = \varepsilon^{\nu} \tilde{T}_{12} \sin k_0 x_0 \sin k_0 y_0 + \cdots,$$

https://doi.org/10.1017/S0022112000002135 Published online by Cambridge University Press

where $v > \frac{1}{4}$. The following expansion is equivalent to the linear stability analysis of the two-dimensional rolls, and it will not be necessary to specify the particular value of v. (The assumption about the scaling of a perturbation as ε^v is guided only by the consideration that the asymptotic expansion in one parameter is usually more rigorous than the expansion in two parameters and more convenient as well.)

When the temperature $T = T_{basic} + T_{c-r} + T_{int}$ is substituted in the advection–diffusion equation (2.1c) and the salinity is considered similarly, then at order $\varepsilon^{v+1/2}$ we obtain

$$\tilde{S}_2 = \tilde{T}_2, \quad \tilde{w}_2 = \left(\frac{\partial^2}{\partial z_0^2} - k_0^2\right)\tilde{T}_2,$$

$$\tilde{S}_{12} = \tilde{T}_{12}, \quad \tilde{w}_{12} = \left(\frac{\partial^2}{\partial z_0^2} - 2k_0^2\right)\tilde{T}_{12},$$

where $\varepsilon^v \tilde{S}_2 \sin k_0 y_0$, $\varepsilon^{v+1/2}\tilde{w}_2 \sin k_0 y_0$ are the leading-order salinity field and the vertical velocity field in the 'cross-roll' mode, $\varepsilon^v \tilde{S}_{12} \sin k_0 x_0 \sin k_0 y_0$, and $\varepsilon^{v+1/2}\tilde{w}_{12} \sin k_0 x_0 \sin k_0 y_0$ are those fields in the 'interaction' mode. The order-$\varepsilon^{v+3/4}$ balances in the continuity equation (2.1b) and in the vorticity equation ($\partial u/\partial y - \partial v/\partial x = 0$) determine the order-$\varepsilon^{v+1/2}$ horizontal velocity components. For the 'cross-roll' mode we have

$$v = \varepsilon^{v+1/2}\tilde{v}_2 \cos k_0 y_0 + \cdots, \quad \tilde{v}_2 = \left(k_0^{-1}\frac{\partial^3}{\partial z_0^3} - k_0\frac{\partial}{\partial z_0}\right)\tilde{T}_2, \quad u = 0$$

at this order; and for the 'interaction' mode we have

$$u = \varepsilon^{v+1/2}\tilde{u}_{12} \cos k_0 x_0 \sin k_0 y_0 + \cdots, \quad \tilde{u}_{12} = \frac{1}{2k_0}\left(\frac{\partial^3}{\partial z_0^3} - 2k_0^2\frac{\partial}{\partial z_0}\right)\tilde{T}_{12},$$

$$v = \varepsilon^{v+1/2}\tilde{v}_{12} \sin k_0 x_0 \cos k_0 y_0 + \cdots, \quad \tilde{v}_{12} = \frac{1}{2k_0}\left(\frac{\partial^3}{\partial z_0^3} - 2k_0^2\frac{\partial}{\partial z_0}\right)\tilde{T}_{12}.$$

Now consider the $O(\varepsilon^{v+1})$ terms in the advection–diffusion of the temperature equation (similar analysis of the salinity equation would be redundant since we showed that $S = T$ at the leading order in all the modes). If the time derivatives of (T, S) are non-negligible at this order, then the time should be rescaled as $t = \varepsilon^{-1}t_0$. When the terms proportional to $\sin k_0 x_0 \sin k_0 y_0$ and the terms proportional to $\sin k_0 y_0$ in the temperature equation are isolated (at order ε^{v+1}), after extensive algebra we obtain a closed system of the rescaled equations:

$$\left.\begin{aligned}
&\frac{\partial \tilde{T}_{12}}{\partial t_0} + (\mathrm{D}^2 - k_0^2)T_1 \cdot \mathrm{D}\tilde{T}_2 + \mathrm{D}T_1 \cdot (\mathrm{D}^2 - k_0^2)\tilde{T}_2 = 0,\\
&\frac{\partial \tilde{T}_2}{\partial t_0} + \tfrac{1}{2}(\mathrm{D}^3 - k_0^2\mathrm{D})T_1 \cdot \tilde{T}_{12} + \tfrac{1}{2}(\mathrm{D}^2 - k_0^2)T_1 \cdot \mathrm{D}\tilde{T}_{12}\\
&\quad + \tfrac{1}{4}T_1 \cdot (\mathrm{D}^3 - 2k_0^2\mathrm{D})\tilde{T}_{12} + \tfrac{1}{2}\mathrm{D}T_1 \cdot (\mathrm{D}^2 - 2k_0^2)\tilde{T}_{12} = 0,
\end{aligned}\right\} \tag{4.3}$$

where $\mathrm{D} \equiv \partial/\partial z_0$. This system, linear with respect to $(\tilde{T}_{12}, \tilde{T}_2)$, describes the instability of the basic steady state T_1 with respect to the (small) 'cross-roll' perturbation.

The system (4.3) was integrated numerically to determine whether steady states T_1 are unstable. We used the steady solutions of (3.10) obtained numerically in § 3.1 for T_1, initiated calculations with a random perturbation for $(\tilde{T}_{12}, \tilde{T}_2)$, and integrated (4.3) using a pseudo-spectral method similar to the one employed previously. For all the values of μ considered, the norm of the perturbation $E = \sqrt{\langle T_2^2 \rangle}$ was growing in

https://doi.org/10.1017/S0022112000002135 Published online by Cambridge University Press

	$R = 2.6$	$R = 2.2$	$R = 1.6$
$\mu = 1:20$	Roll	Roll	Square cell
$\mu = 1:40$	Roll	Square cell	Square cell
$\mu = 1:80$	Square cell	Square cell	Square cell

TABLE 3. Stability of two-dimensional solutions. The final planform.

time, i.e. the average growth rate

$$\tilde{\lambda} = \lim_{\Delta \to \infty} \left(\frac{1}{\Delta} \ln \frac{E(t_0 + \Delta)}{E(t_0)} \right)$$

was always positive. Furthermore, this growth rate monotonically increased when μ was decreased, which implies that tall rolls are strongly unstable with respect to the cross-roll perturbations. The 'fastest growing modes' (not shown), which eventually dominated after the system (4.3) was integrated in time (starting from a random initial perturbation), had large amplitudes in the vicinity of the boundary layers near $z = 0, H$ and relatively small amplitudes in the interior. This indicates that the instability has a quasi-local character and is related to the large vertical gradients of the basic state in the boundary layers.

Note that if one considers only the solutions in which variations in z occur (uniformly) on much larger scales than the variations in x (i.e. $D \ll k_0$) and neglects the corresponding terms in (4.3), then these equations reduce to a *stable* system, because there would be a positive definite quadratic norm of a perturbation which is conserved: $(\partial/\partial t_0)\langle T_1^{3/2}(\tilde{T}_2^2 + \tilde{T}_{12}^2)\rangle = 0$. The assumption $\partial/\partial x \gg \partial/\partial z$, used in most of the previous nonlinear theories for salt fingers, apparently accounts for the incorrect result that two-dimensional motion is stable (as in the Proctor & Holyer 1986 model). The instability of the two-dimensional fingers with the boundary layers where $\partial/\partial x \sim \partial/\partial z$ shows how sensitive the double-diffusive system is to a proper resolution of the small vertical scales.

4.2. *Numerical calculations for finite* ε

The foregoing asymptotic theory is limited to the demonstration of the linear instability of two-dimensional motion (for $\varepsilon \to 0$), and therefore it is possible that the planform realized in the experiments may be some combination of rolls and cells. (In connection with the latter possibility we remark that there is experimental evidence for realization of the complicated structures that cannot be clearly identified with either rolls or cells as in Chen & Sandford (1976).) In order to determine the actual planform of the fingers we use numerical calculations for the full high-Prandtl-number equations (2.1). These calculations were initiated using the asymptotic steady solution (3.11), (3.13) for various (finite) ε and μ. We used $(\alpha, \beta) = (0.995, 0.1)$ in (3.13), which corresponds to a roll oriented in the y-direction slightly perturbed by a 'cross-roll' disturbance. The results of these experiments are summarized in table 3, which shows that for some values of (R, μ) the three-dimensional instability results in a complete disruption of the rolls and in the transition to a predominantly square cell pattern, while for other cases the planform remains quasi-two-dimensional (with only a small variation in the y-direction).

Figure 5(a, b, c) shows such a transition from a 'roll' to a 'square cell' structure for the $(\mu, R) = (1:40, 2.2)$ calculation. This transition did not occur at the same time

https://doi.org/10.1017/S0022112000002135 Published online by Cambridge University Press

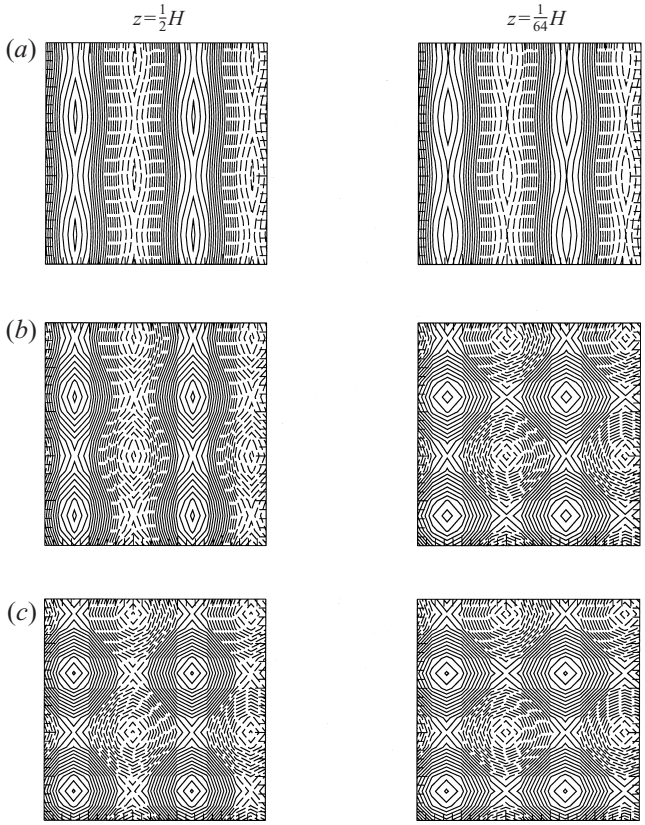


FIGURE 5. Transition from rolls to square cells. Numerical calculations were initiated by the two-dimensional asymptotic steady state with $R = 2.2, \mu = 1:40$ perturbed by a small cross-roll mode (see the text). (*a*) Horizontal cross-sections of the temperature field across the boundary layer ($z = \frac{1}{64}H$) and across the interior region ($z = \frac{1}{2}H$) initially ($t = 0$). (*b*) The same as in (*a*) but for $t = 400$. The boundary layer cross-section transforms to the square cell type structure, while the interior cross-section still resembles the rolls. (*c*) The same for $t = 4600$. Transition to the square cell planform is now completed at all levels.

at different levels in z. The three-dimensional character appears first in the boundary layers near $z = 0, H$ (see figure 5*b*), as expected from the structure (not shown) of the fastest growing cross-roll perturbations (§ 4.1); subsequently the interior region also transforms into a three-dimensional cell (figure 5*c*). Such effects also occurred in the experiments (not shown) in which rolls were perturbed only by a small-scale random noise. Although the precise conditions (table 3) favourable for the square cells (rolls) are yet to be explained, the apparent tendency for formation of the significantly three-dimensional fingers when the aspect ratio (μ) is small is consistent with the considerations in § 4.1 which show that the growth rate of the three-dimensional instability increases with H.

Especially noteworthy is the fact that in the parameter range corresponding to a typical laboratory salt–sugar experiment, namely $R \sim 1.6, \mu \sim 1:40$ (as cited by Radko & Stern 1999), the observed square cells are clearly preferred in our model (see table 3). We also reproduced that $(R, \mu) = (1.6, 1:40)$ experiment by initiating calculations with a small-scale random noise, and again obtained remarkably regular fingers with an almost perfect square cell structure (not shown). The foregoing analysis suggests

https://doi.org/10.1017/S0022112000002135 Published online by Cambridge University Press

μ	1 : 10	1 : 30	1 : 40	1 : 50	1 : 100
$-\langle\overline{wT}\rangle$	1.14	5.14	7.66	10.4	22.55
C (cm s^{-1})	4.9×10^{-4}	5.1×10^{-4}	5.1×10^{-4}	5.2×10^{-4}	4.4×10^{-4}

TABLE 4. The values of C for the steady states consisting of one finger pair, $R = 1.6$.

that the observed (Shirtcliffe & Turner 1970) preference for the square cell planform might be caused by the instability of the solutions with non-square planforms that occurs for the particular values of (R, μ). We should also mention that the time involved in the transition from one planform to another ($\sim \mu^{-2}\varepsilon^{-1}$) is very large because the 'interaction' term $\tilde{T}_{12}$ is typically quite small (as indicated in § 3.2); this explains why we were able to obtain numerically (§ 2) both steady rolls and steady square cells, even when the latter solutions are formally unstable.

5. The $\Delta S^{4/3}$ flux law

5.1. *Flux law coefficient as determined from the numerical 'rigid lid' calculations*

As previously mentioned, most of the laboratory experiments show that the salt flux through an interface containing salt fingers can be parametrized as

$$\langle\overline{wS}\rangle_{dim} = C(\Delta S^*)^{4/3}, \tag{5.1}$$

where ΔS^* is the given (dimensional) S-difference across the interface, and C depends only on the density ratio (for fixed values of the molecular diffusivities). The 4/3 law was originally suggested by Turner (1967) as a plausible extension of results from turbulent thermal convection, and, as Taylor & Veronis (1996) pointed out, a direct application of it to the quite different physics of the double-diffusive convection may be suspect. Thus, an additional justification is needed to use the 4/3 law for the salt-finger interface. One of the purposes of the following theory is to verify this similarity law for the salt fingers in the 'rigid lid' configuration.

One fundamental difference between our rigid lid model and the laboratory experiment is that in the latter case the equilibrium height of the finger interface is independent of its initial value and adjusts to a definite function of $(\Delta T^*, \Delta S^*)$. In our model, however, the height of a finger zone is a free parameter, which we can vary even for fixed $\Delta T^*, \Delta S^*$, and therefore on purely dimensional grounds we might expect that C in our model depends on the distance ($H \sim \mu^{-1}$) between the rigid boundaries. In order to determine the extent of this dependence, the flux law coefficient C in (5.1) is first expressed in terms of our non-dimensional quantities (R, H, and flux $\langle\overline{wT}\rangle$):

$$C = \frac{\langle\overline{wS}\rangle_{dim}}{(\Delta S^*)^{4/3}} = \left(\frac{gk_T^2}{\nu}\right)^{1/3} \frac{\gamma^{-1}\langle\overline{wT}\rangle}{H^{4/3}} R^{4/3}. \tag{5.2}$$

For $R = 1.6$ and various μ (or H) we numerically computed the three-dimensional one-finger-pair equilibrium fluxes, and then C (with positive sign) was obtained from (5.2) using $k_T = 1.5\times10^{-5}$ cm^2 s^{-1} for the salt–sugar experiment, $\nu = 1.3\times10^{-2}$ cm s^{-1}, and $g = 980$ cm s^{-2}. The results are in table 4.

Thus we have the important numerical result that even in the rigid lid model the value of the flux law coefficient is insensitive to changes in the height of a finger layer, and is almost uniquely determined by R. A theoretical explanation of this property

https://doi.org/10.1017/S0022112000002135 Published online by Cambridge University Press

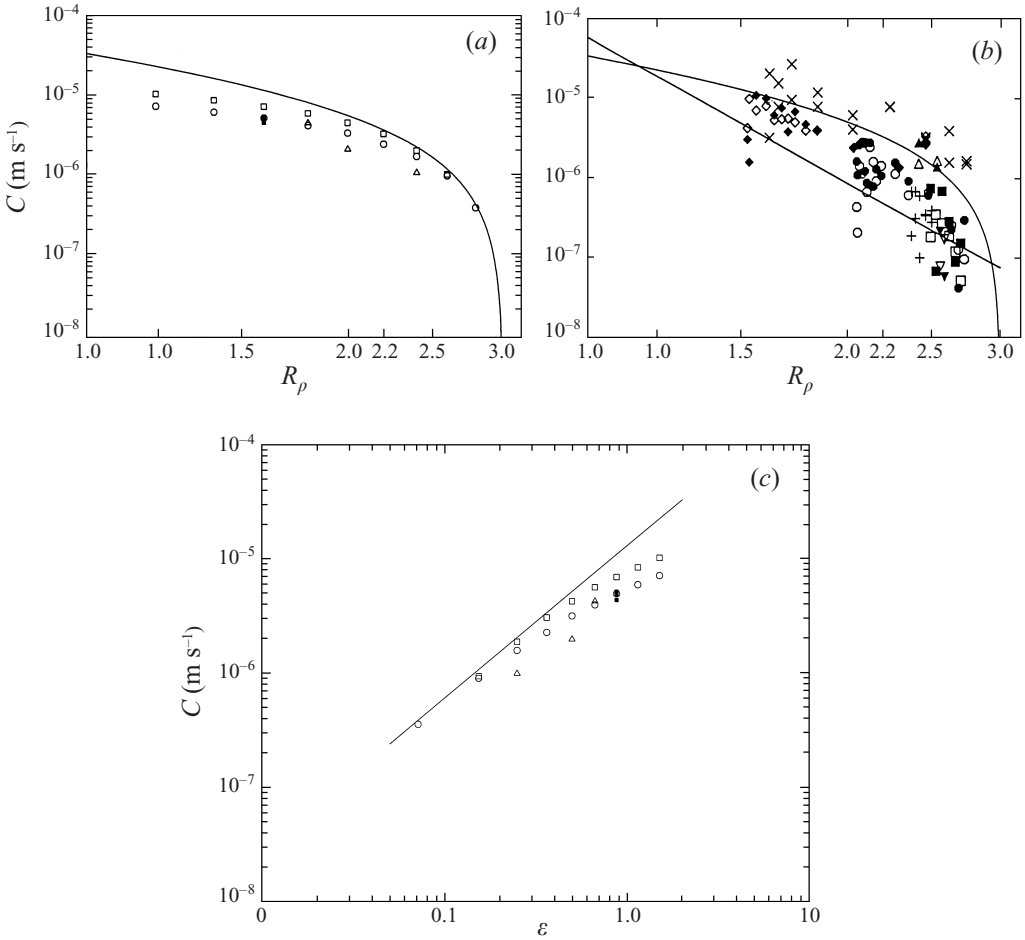


FIGURE 6. Flux law constant C as a function of $R_\rho \equiv R = \tau^{-1}(1+\varepsilon)^{-1}$ in the rigid lid model and in the laboratory experiments. (*a*) Comparison of the asymptotic theory (5.3) (solid curve) with the results of numerical calculations symbols: circle, two-dimensional calculations with one finger (see text); open square, three-dimensional calculations with 5×5 fingers; triangle, two-dimensional experiments with 10 fingers; filled square, two-dimensional experiments with one finger at $R = 1.6$ and various aspect ratios. Experiments marked by circles, open squares and triangles are for $\mu = 1:10$. The theoretical estimate agrees with the numerics within a factor of 2. (*b*) Modified from figure 7 in Taylor & Veronis (1996) (the straight line is an average of the other laboratory experiments). The theoretical curve in (*a*) is superimposed on the results of the laboratory experiments. Qualitative agreement between these estimates suggests that the dynamics of the finger zone in the rigid lid model and in the laboratory experiments (where the finger zone is sandwiched between the two well mixed reservoirs) are similar. (*c*) C from numerical experiments as a function of ε in logarithmic coordinates. The same symbols as in (*a*) are used for the data points. For small values of ε the numerical C agree well with the asymptotic ($\varepsilon \to 0$) power law (5.3) presented by a solid line.

is deferred to § 5.3, but first we will compare $C(R)$ in our rigid lid model with the experimental data (Taylor & Veronis 1996).

5.2. *Comparison of the numerical, analytical, and laboratory results*

In figure 6(*a*) we plot $C(R)$ obtained from several numerical rigid lid experiments which included the following groups:

https://doi.org/10.1017/S0022112000002135 Published online by Cambridge University Press

(i) two-dimensional experiments with one pair of fingers (i.e. the width of the computational domain is approximately equal to the fastest growing wavelength (2.2)), marked by circles;

(ii) two-dimensional experiments with 10 pairs (the width of computational domain exceeded the fastest growing wavelength by a factor of 10) indicated by triangles;

(iii) three-dimensional experiments with 5×5 pairs of fingers indicated by open squares;

(iv) two-dimensional experiments in table 4, indicated by the filled squares.

All the experiments except those in group (iv) were for the aspect ratio $\mu = 1:10$, and the most relevant to observations are the three-dimensional multiple finger calculations (group iii).

It is of interest to compare these calculations with the asymptotic ($\varepsilon \to 0$) theory. When the scalings in § 3 are used to simplify (5.2) the result is

$$C(R) = \varepsilon^{4/3} C_0, \tag{5.3}$$

where $C_0 = (gk_T^2/\nu)^{1/3}\tau^{-4/3}\langle\overline{w_0 T_0}\rangle/H_0^{4/3}$. For the $\mu = 1:10$ case in figure 3(a,b) (for which $\langle w_0 T_0\rangle = -1.67$, and $H_0 = \pi 3^{1/4}\mu^{-1}$) we obtain $C_0 \approx 1.3 \times 10^{-3}$, and the values of C_0 for $\mu = 1:5, 1:20$, and $1:40$ are very close to that for $\mu = 1:10$. The extrapolated asymptotic relation (5.3) in figure 6(a) is qualitatively consistent with the numerical calculations; the extrapolation overestimates C approximately by a factor of 2 for small values of R, but provides correct values for larger R (for which the aforementioned asymptotic $\varepsilon \to 0$ is most appropriate). The agreement of the curve with the group (iii) three-dimensional calculations is especially noteworthy.

In figure 6(b) (modified from Taylor & Veronis 1996) we superimposed our analytical expression (5.3) for the rigid lid model on the data obtained by Taylor & Veronis in a series of laboratory experiments. The most interesting and important result in figure 6(b) is that the actual values of C in the laboratory experiments are consistent with the theoretical $C(R)$ in our rigid lid model, and the former values agree even better with our numerical calculations (see the data for group (iii) in figure 6a). These two theoretical estimates not only correctly predict the order of magnitude and the average slope of the laboratory $C(R)$ curve but they also capture the local increase of the slope for large R and decrease of the slope at the lower R.† Such an agreement implies that the basic physics involved in the equilibration of fluxes in the laboratory experiment is described by our simple rigid lid model, in which the vertical velocity is assumed to be zero at the top and bottom of the finger interface. The main reason for that (as was mentioned in the preliminary calculation of Radko & Stern 1999) may be that in the laboratory experiment the vertical velocity is substantially reduced when the particles penetrate the thin transition layer separating the finger interface from the well mixed layer.

The plot of $C(\varepsilon)$ from the numerical calculations in logarithmic coordinates (see figure 6c) demonstrates a good agreement with the theoretical power law (5.3) for the moderately small values of ε.

5.3. *Rationalization of the flux law for the rigid lid calculations*

In order to show why the flux law coefficient C in our rigid model is not sensitive to the changes in the distance between the rigid boundaries (see the table 4) we fix

† It should be mentioned that although Griffiths & Ruddick (1980) obtained lower values of C than Taylor & Veronis (1996), they concentrated on the parameter range corresponding to smaller R, while our asymptotic result in figure 6(b) and Taylor & Veronis's data correspond to larger values of R. Comparison with Taylor & Veronis is therefore more appropriate.

https://doi.org/10.1017/S0022112000002135 Published online by Cambridge University Press

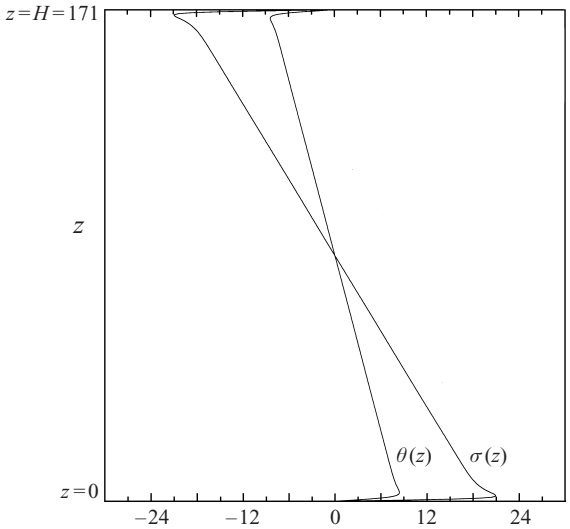


FIGURE 7. Mean fields (θ, σ) for the two-dimensional steady state with $(\mu, R) = (1:40, 1.6)$. Note the remarkably uniform gradients of $(0, \sigma)$ in most of the interior (see text) and the well-defined boundary layers at the top $(z = H)$ and at the bottom $(z = 0)$.

R and examine how the increase of the distance between the rigid boundaries affects our steady solutions. We should mention that when H is too large (for example, when $\mu < 1:200$ for $R = 1.6$) numerical experiments (not shown) reveal that the regular finger pattern (such as in figure 1) changes to a more irregular structure, an effect apparently related to the behaviour found in an unbounded model (see Stern & Radko 1998; Radko & Stern 1999). This regime will not be considered below, and we will assume that H is such that the fingers are steady and regular (even when the formal limit $H \to \infty$ is computed).

Before proceeding further we remind the reader that there are significant differences in the detailed structure of the single-finger-pair solutions (e.g. figure 1), for which the periodic boundary conditions in x and y are imposed at the distances approximately corresponding to the fastest growing (on the unperturbed linear gradient) modes, and the 'multiple-finger' numerical solutions (e.g. figure 2) obtained with large computational domains. As was mentioned in § 2 the latter solutions are less regular spatially and not quite steady. However, the purpose of this section is to explain qualitatively the dependence of fluxes on H, and their order of magnitude, and therefore we consider a much simpler one-finger-pair model. (Note that the numerically obtained fluxes in the multiple-finger runs and the one-finger calculations differ no more than by a factor of 2).

All the numerically obtained one-finger-pair steady states look very similar (unless μ is exceedingly small, as mentioned above). The temperature field (similar to figure 1), as well as the salinity field, consists of a remarkably uniform interior with

$$\frac{\partial}{\partial z}(T', S', w) \approx 0, \tag{5.4}$$

bounded at the top (near $z = H$) and at the bottom (near $z = 0$) by well-defined boundary layers. As was shown previously (§ 3), such a steady state is achieved by the modified mean field (θ, σ). The gradients of the mean fields $(\partial/\partial z)(\theta, \sigma) \equiv (a_i, b_i) \approx$

https://doi.org/10.1017/S0022112000002135 Published online by Cambridge University Press

const. are also remarkably uniform in the interior as shown in figure 7 for a two-dimensional steady state with $(\mu, R) = (1:40, 1.6)$. In order to consider the equilibrium state of long laminar fingers in the interior region we substitute (5.4) in (2.1) to obtain

$$\frac{\partial \bar{T}_{new}}{\partial z} w = \nabla_h^2 T', \quad \frac{\partial \bar{S}_{new}}{\partial z} w = \tau \nabla_h^2 S', \quad \nabla_h^4 w = \nabla_h^2 (S' - T'), \tag{5.5}$$

and this implies that the fingers which are fastest growing on the original (unperturbed) T, S gradients should be marginally unstable on the *new* uniform gradient $(\partial \bar{T}_{new}/\partial z = 1 + \partial\theta/\partial z,\ \partial \bar{S}_{new}/\partial z = R^{-1} + \partial\sigma/\partial z)$ in the interior (a similar idea was also used by Schmitt 1979). When the wavenumber of the fastest growing finger k_f (c.f. (2.2)) is used in (5.5), the result is

$$\left[\frac{1}{\tau}\left(\frac{1}{R} + b_i\right) - (1 + a_i)\right] = k_f^4 = \frac{1}{3}\left(\frac{1}{R\tau} - 1\right), \tag{5.6}$$

where $a_i = \partial\theta/\partial z$ and $b_i = \partial\sigma/\partial z$ are the interior mean-field gradients. (Note that in the one-finger-pair model the linearly fastest growing finger retains its wavenumber in the equilibrium state, whereas in the multiple-finger models this may not be exactly correct.)

The steady mean-field equations obtained by averaging (horizontally) the advection–diffusion equations (2.1c, d) are

$$\frac{\partial}{\partial z}\theta = [(\overline{wT'}) - \langle \overline{wT'} \rangle], \quad \frac{\partial}{\partial z}\sigma = \tau^{-1}[(\overline{wS'}) - \langle \overline{wS'} \rangle]. \tag{5.7}$$

The ratio of these at the rigid walls (where $w = 0$) yields

$$\frac{a_b}{b_b} = \tau\gamma, \tag{5.8}$$

where $a_b \equiv \partial\theta/\partial z|_{z=0}$, $b_b \equiv \partial\sigma/\partial z|_{z=0}$, and $\gamma \equiv \langle \overline{wT'} \rangle / \langle \overline{wS'} \rangle$ is the flux ratio.

Consider the simplified model for the structure of the temperature and salinity mean fields in figure 8, in which the boundary layers are assumed to be purely conductive with $(\partial/\partial z)(\theta, \sigma) \equiv (a_b, b_b) \approx$ const, and the interior gradients are uniform as well. We also use the fact that the boundary layer thickness d estimated for the temperature field is close to that for the salinity, which was observed in all our numerical experiments (see figure 1a, b) and explained in the asymptotic theory (§ 3). Since the total variation in (θ, σ) across the entire layer $(0 < z < H)$ vanishes, the mean fields in the boundary layer are related to that in the interior by

$$\frac{a_i}{a_b} = \frac{b_i}{b_b} = -\frac{2d}{H - 2d}. \tag{5.9}$$

The solution of the four equations (5.6), (5.8), (5.9) results in an expression for the steady heat flux:

$$-\langle \overline{wT} \rangle = a_b = \frac{2}{3}\frac{(R^{-1} - \tau)\gamma\tau}{(1 - \gamma\tau^2)}\left[\frac{H}{2d} - 1\right], \quad a_i = -\frac{2}{3}\frac{(R^{-1} - \tau)\gamma\tau}{(1 - \gamma\tau^2)}. \tag{5.10a, b}$$

The flux ratio $0 < \gamma < 1$ is known to be nearly constant; in the sugar–salt laboratory experiments (and in all our numerical experiments) it is bounded by $0.7 < \gamma < 1$, and therefore γ in (5.10) does not depend significantly on H. For $R = 1.6$, for example, various aspect ratios ranging from $\mu = 1:10$ to $1:100$ gave values of γ that differ by less than 3%. In order to estimate how the heat flux (and C) depends on H in (5.10),

https://doi.org/10.1017/S0022112000002135 Published online by Cambridge University Press

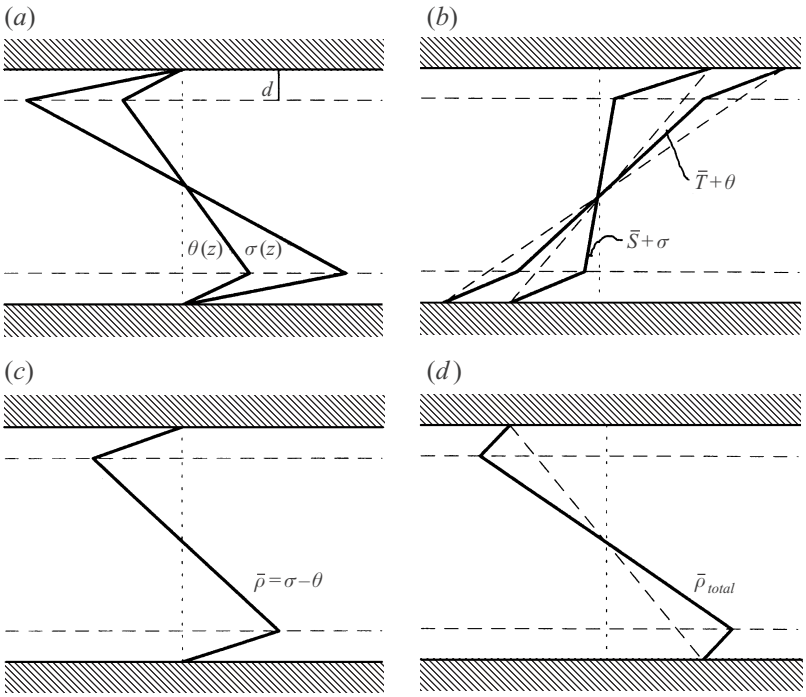


FIGURE 8. Schematic diagram of the mean fields in a rigid lid steady state. (*a*) (θ, σ): departure of the mean temperature and salinity fields from the linear gradients. Compare with figure 7. (*b*) The *total* mean fields $\bar{T}_{total} = \bar{T} + \theta, \bar{S}_{total} = \bar{S} + \sigma$; dashed lines correspond to the original linear gradients $\bar{T}, \bar{S}$. (*c*) The mean density $\bar{\rho} = \sigma - \theta$ (or, more correctly, departure of the mean density from the original linear gradient). (*d*) The total mean density field, which consists of the original linear gradient (dashed line) and its modification due to the salt fingering (shown in *c*).

it only remains to determine the thickness of the boundary layer d as a funtion of H. Since our previous numerical results suggest that as we increase H the boundary layer thickness decreases slowly and the fluxes increase (see table 4), we tentatively assume and subsequently verify that when $H \to \infty$, $d \to 0$ and $(a_b, b_b) \to \infty$ (for fixed ε).

Let us assume (by extrapolating the asymtotic considerations in § 3 to finite ε) that in the steady state the vertical advection of mean field is approximately balanced by the diffusive terms $(\nabla^2 T', \tau \nabla^2 S')$. Then for the boundary layer $0 < z < d$ we have

$$\left.\begin{aligned} (1 + a_b)w &\sim \nabla^2 T', \\ (R^{-1} + b_b)w &\sim \tau \nabla^2 S', \\ \nabla^4 w &= \nabla_h^2 (S' - T'). \end{aligned}\right\} \tag{5.11}$$

Eliminating T' and S' in (5.11) results in

$$\nabla^6 w \sim \nabla_h^2 ([R^{-1}\tau^{-1} - 1 + \tau^{-1} b_b - a_b] w). \tag{5.12}$$

If a_b increases as $H \to \infty$, then $(R^{-1}\tau^{-1} - 1)$ in (5.12) can be neglected, and when (5.8) is used (5.12) becomes

$$\nabla^6 w \sim (\gamma^{-1}\tau^{-2} - 1) a_b \nabla_h^2 w. \tag{5.13}$$

Since the horizontal scale of fingers is independent of H whereas $d^{-1} \to \infty$ has been

https://doi.org/10.1017/S0022112000002135 Published online by Cambridge University Press

assumed, (5.13) yields

$$d^{-6} \sim k_f^2(\gamma^{-1}\tau^{-2} - 1)a_b. \tag{5.14}$$

Solving (5.14) and (5.10*a*) for d and a_b as a function of H (or μ) we finally obtain

$$d \sim \left[\frac{3}{Hk_f^2\varepsilon}\right]^{1/5}, \tag{5.15a}$$

$$-\langle\overline{wT'}\rangle = a_b \sim \frac{\varepsilon\gamma\tau^2}{3^{1.2}(1-\gamma\tau^2)}H^{6/5}(k_f^2\varepsilon)^{1/5} \sim \frac{(2\pi)^{6/5}\gamma\tau^2}{3(1-\gamma\tau^2)}\mu^{-6/5}\varepsilon. \tag{5.15b}$$

These two results confirm the assumption that as H increases the (non-dimensional) thickness of the boundary layer decreases and the fluxes increase. The foregoing theory involved several order-of-magnitude approximations and therefore it is not surprising that the coefficient in (5.15*b*) is overestimated by a factor of 2.5 (relative to the numerics). However, the power laws in (5.15) are consistent with our previous results (§ 3) which suggest that the fluxes are proportional to ε (for fixed μ) and to $\mu^{-6/5}$ (for fixed ε). As far as the fully nonlinear numerical calculations are concerned, the least-square fit of the straight line to the data in table 4 plotted in logarithmic coordinates yields the value of -1.31 for the exponent. However, when the estimate is made excluding the largest $\mu = 1:10$ (since $\mu \to 0$ in the foregoing theory) the value of the slope is -1.22, which agrees well with our theory ($\mu^{-6/5}$).

From (5.15) and (5.2) we see how the flux law coefficient depends on H:

$$C = \left(\frac{gk_T^2}{\nu}\right)^{1/3}\frac{R^{4/3}}{\gamma}\frac{a_b}{H^{4/3}} \sim \left(\frac{gk_T^2}{\nu}\right)^{1/3}F(R)H^{-2/15}, \tag{5.16}$$

where the coefficient

$$F(R) = R^{4/3}\frac{\varepsilon\tau^2}{3^{1.2}(1-\gamma\tau^2)}(k_f^2\varepsilon)^{1/5}$$

depends only on R. Equation (5.16) for C implies a very weak dependence on H: a ten-fold increase in H results in only a 26% decrease of the flux law coefficient. This explains why C in our numerical experiments (table 4) is insensitive to the changes in H, and why the comparison of $C(R)$ in our model with the experimental values could be meaningfully performed without using a particular (corresponding to the experiment) value of H.

Finally, let us rewrite the relation (5.16) in terms of (dimensional) H^*, i.e. estimate how the flux law constant C will change if we fix $(\Delta T^*, \Delta S^*)$ and increase only the (dimensional) height of the layer. Since the length unit is $\lambda = (k_T\nu/g\bar{T}_z^*)^{1/4}$ (see § 2) we have

$$H = (H^*)^{3/4}\left(\frac{g\Delta T^*}{k_T\nu}\right)^{1/4}, \tag{5.17}$$

and the substitution of (5.17) in (5.16) results in

$$C \approx F(R)\frac{g^{3/10}k_T^{7/10}}{\nu^{3/10}}(H^*)^{-1/10}(\Delta T^*)^{-1/30}. \tag{5.18}$$

The exponents $-1/10$ and $-1/30$ in (5.18) correspond to extremely weak dependences and, therefore, our C is effectively a function of the density ratio R only. This proves that the 4/3 flux law is a sufficiently accurate approximation for a rigid lid model.

https://doi.org/10.1017/S0022112000002135 Published online by Cambridge University Press

6. The vertical extent of the finger zone

As previously mentioned, H^* is a free parameter in our rigid lid model, whereas in most laboratory experiments (Linden 1978) the equilibrium height of a finger zone cannot be controlled but is a function of $(\Delta T^*, \Delta S^*)$. (The rare exception occurs for very weak fingers in the run-down sugar–salt experiments, such as described by Taylor & Veronis 1996.) Thus, in order to explain the observed height of a 'strong' finger zone we have to incorporate into our rigid lid model additional ideas about the mechanism that limits the vertical scale of the experimentally observed fingers. Previous theories (Stern & Turner 1969; Kunze 1987) assumed that the limitations on the thickness of the finger zone result from various instabilities of long fingers (e.g. collective instability). The significance of Stern's (1969) collective instability effect for layer formation was questioned by Shen (1989) on the basis of his numerical calculations. Shen suggested that the breakup of fingers occurs due to the formation of local inversions of the density stratification in the transition region at the edges of the finger interface. In this section we will also argue that the mechanism which stops the (vertical) spreading of the finger interface in the laboratory experiments is directly related to the formation of thin boundary layers which, for certain values of the parameters, may exhibit a strong *local* instability (different from that previously associated with the interior of finger zone).

As previously mentioned, observations show that when particles penetrate from the finger interface into the well mixed layer they significantly slow down in thin 'transition' zones (see the shadowgraphs in Linden 1978). The resulting $O(1)$ decrease in the convective fluxes $(\overline{wT}, \overline{wS})$ in these thin layers is compensated by the conductive fluxes $(\partial\theta/\partial z, \tau\partial\sigma/\partial z)$, which requires a large positive salinity gradient in the transition layer. Such well-defined boundary layers also occur in all our rigid lid numerical experiments. They are steady and regular for moderate heights of the finger zone (see figure 9*a* for the $(R, \mu) = (1.6, 1:50)$ two-dimensional case); however, when we increase the height of the finger zone, these boundary layers become irregular and unsteady, as shown by the calculation in figure 9(*b*) in which H is doubled $(\mu = 1:100)$.

In order to determine conditions for this new instability of the boundary layer we will make the 'marginal instability' assumption† that it occurs when a *local* thermohaline Rayleigh number

$$Ra = \frac{g(d^*)^4}{\nu}\left(\frac{1}{k_s}\left(\frac{\partial \bar{S}_{total}}{\partial z}\right)_{dim} - \frac{1}{k_T}\left(\frac{\partial \bar{T}_{total}}{\partial z}\right)_{dim}\right), \tag{6.1a}$$

exceeds a certain critical value (tentatively estimated as $Ra_c \sim 1000$), where d^* is the dimensional boundary layer thickness. Note that this expression is a valid instability criterion for the thermohaline case of a gravitationally stable $(\partial\bar{\rho}^*_{total}/\partial z < 0)$ layer, and for a 'top-heavy' layer of fluid $(\partial\bar{\rho}^*_{total}/\partial z > 0)$ as well. In the latter case the term due to the temperature gradient in (6.1*a*) will be significantly less than the term due to the salinity gradient, and the resulting instability will be similar to Rayleigh convection.

We now show that the foregoing assumption is also supported by the numerical calculations in figure 9(*a*, *b*). In our non-dimensional variables the definition (6.1*a*)

† The analogous assumption for the convection from a heated surface was made by Howard (1964), who estimated the maximum height of the thermal boundary layer (and, subsequently, the heat flux) by setting its local $Ra \sim 1000$, and obtained a reasonable agreement with the experiments.

https://doi.org/10.1017/S0022112000002135 Published online by Cambridge University Press

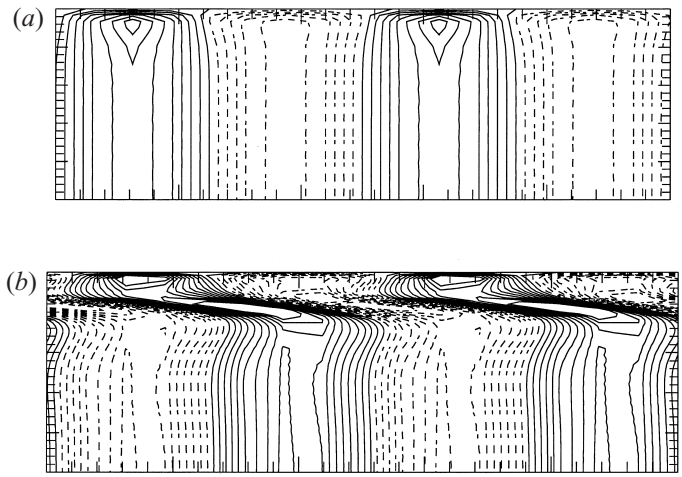


FIGURE 9. Isopleths of the temperature in the boundary layer near $z = H$ for the two-dimensional one-finger calculations with $R = 1.6$. (*a*) Aspect ratio is $\mu = 1:50$, the boundary layer Rayleigh number is $Ra = 1440$; (*b*) $\mu = 1:100$, $Ra = 2800$. The boundary layer in (*a*) is stable and laminar, while in (*b*) it is distorted by the local instability. This is related (see the text) to the larger values of the boundary layer Rayleigh number.

becomes

$$Ra = d^4 \left[\tau^{-1}\left(R^{-1} + \frac{\partial\sigma}{\partial z}\right) - \left(1 + \frac{\partial\theta}{\partial z}\right)\right]\Bigg|_{b.l.} = d^4[\tau^{-1}(R^{-1} + b_b) - (1 + a_b)]. \quad (6.1b)$$

From the results in figure 9(*a*) (regular boundary layer), equation (6.1*b*) gives $Ra = 1440$,† and for the state in figure 9(*b*) (unstable boundary layer) $Ra = 2800$. Similar features have been observed in the three-dimensional calculations as well (not shown), which confirms that the *boundary layer* Rayleigh number (6.1*a*) determines a new instability of the thin boundary layers. This point should not be regarded as a mere extension of the well-known laminar instability theory, since the boundary layer instability may be affected by the already existing finite-amplitude salt fingers (which must ultimately be considered in a complete theory).

This new instability of the boundary layers (figure 9*b*) does not penetrate far into the interior because of the (marginally) stable stratification there. The adjacent rigid wall (at $z = 0, H$) also acts to localize this instability, but in the laboratory experiments there is no such wall and thus the local instability in the transition layer penetrate into the well mixed layers. The resulting large-scale turbulent motion in the mixed layers shears away the finger ends from the transition layer (thereby controlling the vertical extent of fingers H). It is important to mention that the Rayleigh number in (6.1*b*) increases with the increase of the height of the finger zone H; this was observed in the numerical calculations and can be explained using our simplified analytical theory in § 5.3 ($d \sim H^{-0.2}, (a_b, b_b) \sim H^{6/5}$, and therefore $Ra \sim H^{0.4}$). Thus, in a laboratory experiment in which the two well-mixed layers of T, S are initially separated only by a sharp interface, the salt fingers can grow in length until their height is such

† Note that since the gradients in the boundary layer are not uniform, unlike that in the classical thermohaline instability problem, the Rayleigh number could be defined in several ways. In this paper we consistently computed d as a distance from the rigid boundary to the nearest extremum of $\theta(z)$ and used the average of gradients at the top and at the bottom of the boundary layer for $(\partial/\partial z)(\bar{T}_{total}, \bar{S}_{total})|_{b.layer}$ in (6.1*a*, *b*).

https://doi.org/10.1017/S0022112000002135 Published online by Cambridge University Press

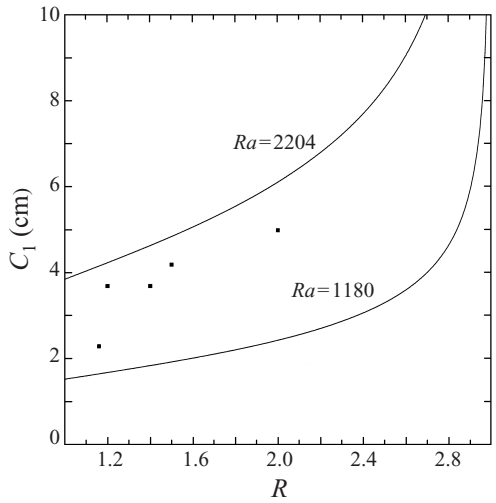


FIGURE 10. Comparison of the theoretical expression for the coefficient C_1 in the one third law (6.6) with the results of the laboratory experiments (Linden 1978). The analytical theory suggests that the values of $C_1(R)$ should be located in the region bounded by the two solid lines; this is consistent with Linden's data presented by the solid squares here. The slope of the theoretical $C_1(R)$ curves is also in apparent agreement with the experimental data.

μ	Ra	H_0
1:5	209	21
1:10	316	41
1:20	540	83
1:40	794	165
1:80	1180	331
1:160	2204	662

TABLE 5. Boundary layer Rayleigh number determined from the asymptotic theory.

that the boundary layer Rayleigh number reaches the critical value. Despite the complexity of the laboratory experiment (compared to our idealized model) we now assume that the previously obtained Rayleigh number condition for the onset of boundary layer instability in the rigid lid model approximately corresponds to that in the laboratory experiment, and the corresponding critical height of the finger layer H_c will be computed accordingly.

On the basis of the calculations in figure 9(a, b) we estimate that the critical value of the boundary Rayleigh number Ra_c is in the range

$$Ra_c \sim 1000\text{–}2000. \tag{6.2}$$

In order to obtain an explicit estimate for H^* as a function of $(\Delta T^*, \Delta S^*)$, corresponding to the critical boundary layer Rayleigh number (6.2) we will use the asymptotic $\varepsilon \to 0$ theory, which was shown (§ 3) to be adequate even for moderately large values of ε. According to this theory (see (3.6)) (6.1b) reduces to

$$Ra = d_0^4 \left[1 + (\tau^{-2} - 1) \frac{\partial \theta_0}{\partial z_0}\bigg|_{b.l.} \right], \tag{6.3}$$

https://doi.org/10.1017/S0022112000002135 Published online by Cambridge University Press

where $d_0^4 = \varepsilon d^4$. The values of $\partial\theta_0/\partial z_0|_{b.l.}$ and d_0 for various μ (and corresponding $H_0 = 3^{-1/4}\mu^{-1}\pi$) were obtained from the asymptotic steady-state (two-dimensional) calculations (i.e. numerical solution of (3.10)), and the resulting Ra computed from (6.3) are listed in table 5. This indicates that $331 < H_0 < 662$ corresponds to the estimated range (6.2) of Ra_c. The corresponding value of $H = H_c$ is then

$$\left.\begin{aligned} H_c &\sim \varepsilon^{-1/4} H_0 \sim 331(R^{-1}\tau^{-1} - 1)^{-1/4} \quad \text{for} \quad Ra = 1180, \\ H_c &\sim 662(R^{-1}\tau^{-1} - 1)^{-1/4} \quad \text{for} \quad Ra = 2204. \end{aligned}\right\} \tag{6.4}$$

Now relate the above non-dimensional $H = H_c$ to the dimensional variables using (5.17) to obtain

$$H^* = C_1(\Delta S^*)^{-1/3}, \tag{6.5}$$

where

$$C_1 = (k_T \nu/g)^{1/3}\, H_c^{4/3} R^{1/3}.$$

We have thereby obtained a similarity law (6.5) in which C_1 is independent of ΔS^* and is a function of (R, τ). Let us compare the values of a coefficient C_1 suggested by our model with the values of C_1 from the laboratory experiments. For the asymptotic theory

$$\left.\begin{aligned} C_1 &\sim \left(\frac{k_T \nu}{g}\right)^{1/3} \frac{2285}{(R^{-1} - \tau)^{1/3}} \quad \text{for} \quad Ra = 1180, \\ C_1 &\sim \left(\frac{k_T \nu}{g}\right)^{1/3} \frac{5751}{(R^{-1} - \tau)^{1/3}} \quad \text{for} \quad Ra = 2204, \end{aligned}\right\} \tag{6.6}$$

and these theoretical relationships are plotted in figure 10. In order to estimate the experimental values of C_1 we used the data for the 'stable runs' obtained by Linden (1978), computed C_1 directly from (6.5), and also plotted the laboratory data in figure 10. It should be noted that the exact values of R and ΔS^* by the time the system reached the quasi-equilibrium state are uncertain in each experiment. We used the data corresponding to the beginning of the experiments, whereas $(\Delta T^*, \Delta S^*)$ may change somewhat by the time the equilibrium is reached (in which case there would be lower values of C_1 and larger values of R). Nevertheless, we are mainly interested here in the order-of-magnitude estimates of the coefficients in the similarity laws, and we see (figure 10) that all the experimental points belong to the area bounded by the two curves approximately corresponding to the estimated range of the critical Rayleigh numbers (6.2).

Now we note that these boundary layers are actually *gravitationally* unstable for conditions typical for the laboratory experiments ($-Nu \geqslant 1$) since

$$\frac{\partial \rho_{total}}{\partial z} = R^{-1} + \frac{\partial \sigma}{\partial z} - \left(1 + \frac{\partial \theta}{\partial z}\right) = (1 - \gamma^{-1}\tau^{-1})\langle \overline{wT} \rangle - (1 - R^{-1}) > 0.$$

and therefore their instability is similar to the 'top heavy' Rayleigh convection (in our case driven by the S-component). The foregoing model of layer formation is, therefore, consistent with Shen's (1989) interpretation of his numerical results, in which he related the formation of the quasi-equilibrium salt finger layers to the appearance of the thin 'gravitationally inverted' zones.

We should also mention that the expressions for the critical height of fingers (6.4) and for the coefficient C_1 in the similarity law (6.5) are singular for $R \to \tau^{-1}$; this may be related to the experimental results of Taylor & Veronis (1996) who suggested that

https://doi.org/10.1017/S0022112000002135 Published online by Cambridge University Press

the similarity law (6.5) fails for sufficiently small $\varepsilon = (R\tau)^{-1} - 1$. (Or, alternatively, our assumption that the amplitude growth of fingers is approximately equilibrated by the mean-field modification may not be satisfied in the fundamentally time-dependent processes observed by Taylor & Veronis.)

7. Conclusions

Numerical integration of the large Prandtl number equations for a rigid lid model, in which the temperature and salinity are prescribed at the top and at the bottom of the computational box, results in steady-state fingers which are almost z-independent in the interior, and which are coupled to boundary layers near the rigid plates ($z = 0, H$). These finite-amplitude numerical solutions are explained analytically using an expansion in which $\varepsilon = (R\tau)^{-1} - 1$ is small (see (3.10)). The equilibration of the linearly growing normal modes is accomplished by the modification of the horizontally averaged temperature and salinity 'mean fields' (as occurs in the classical Rayleigh–Bénard convection problem).

The fluxes in the rigid lid model are adequately described by the 4/3 flux law (5.1), since the dependence of the coefficient C (in the flux law) on the thickness of the finger layer (H^*) is shown to be extremely weak: $C \sim (H^*)^{-0.1}$. The characteristic values of C as well as their strong ($\sim R^{-6}$) dependence on R are found to be consistent with the values of $C(R)$ in the laboratory experiments. This implies that our simple model is able to capture the essential features of the laboratory experiments even though the transition zones that separate the finger layers from the well-mixed reservoirs are not quite rigid (fingers sheared by the large-scale convection can pass through the transition zone separating the finger interface from the well-mixed layers). The laboratory values for the equilibrium height of the finger interface are also explained by assuming that the height of this interface is limited by a new instability of the thin (and usually 'top heavy') boundary layers that form near the interface boundaries ($z = 0, H$). We verify that this instability occurs when the local thermohaline Rayleigh number (based on the thickness of the boundary layer) exceeds a certain critical value.

We also show that for $\varepsilon \to 0$ the two-dimensional salt fingers of the roll type are unstable with respect to the cross-roll perturbations. The finite-amplitude numerical calculations made in a range corresponding to a typical salt–sugar experiment ($R \sim 1.6, \mu \sim 1:40$) with various initial conditions result in formation of steady fingers with a regular square cell planform, consistent with those observed in the laboratory experiments of Shirtcliffe & Turner (1970).

We gratefully acknowledge funding from the National Science Foundation.

REFERENCES

Canuto, C., Hussaini, M. Y., Quarteroni, A. & Zang, T. A. 1987 *Spectral Methods in Fluid Dynamics*. Springer.

Chen, C. F. & Sandford, R. D. 1976 Sizes and shapes of salt fingers near the marginal state. *J. Fluid Mech.* **78**, 601–607.

Griffiths, R. W. & Ruddick, B. R. 1980 Accurate fluxes across a salt–sugar finger interface deduced from direct density measurements. *J. Fluid Mech.* **99**, 85–95.

Howard, L. N. 1964 Convection at high Rayleigh number. *Proc. Eleventh Intl Congr. Applied Mechanics, Munich* (ed. H. Gortler), pp. 1109–1115, Springer.

Kunze, E. 1987 Limits on growing, finite length salt fingers: a Richardson number constraint. *J. Mar. Res.* **45**, 533–556.

https://doi.org/10.1017/S0022112000002135 Published online by Cambridge University Press

Lambert, R. B. & Demenkow, J. W. 1971 On the vertical transport due to fingers in double diffusive convection. *J. Fluid Mech.* **54**, 627–640.

Linden, P. F. 1978 The formation of banded salt finger structure. *J. Geophys. Res.* **83**, 2902–2911.

Malkus, W. V. R. & Veronis, G. 1958 Finite amplitude cellular convection. *J. Fluid Mech.* **4**, 225–260.

Paparella, F. & Spiegel, E. A. 1999 Sheared salt fingers: Instability in a truncated system. *Phys. Fluids* **11**, 1161–1168.

Proctor, M. R. E. & Holyer, J. Y. 1986 Planform selection in salt fingers. *J. Fluid Mech.* **168**, 241–253.

Radko, T. & Stern, M. E. 1999 Salt fingers in three dimensions. *J. Mar. Res.* **57**, 471–502.

Shen, C. Y. 1989 The evolution of the double-diffusive instability: salt fingers. *Phys. Fluids* A **1**, 829–844.

Shirtcliffe, T. G. L. & Turner, J. S. 1970 Observations of the cell structure of salt fingers. *J. Fluid Mech.* **41**, 707–719.

Schmitt, R. W. 1979 The growth rate of super-critical salt fingers. *Deep-Sea Res.* **26A**, 23–40.

Schmitt, R. W. 1994 Double diffusion in oceanography. *Ann. Rev. Fluid Mech.* **26**, 255–285.

Stern, M. E. 1969 The collective instability of salt fingers. *J. Fluid Mech.* **35**, 209–218.

Stern, M. E. & Radko, T. 1998 The salt finger amplitude in unbounded T–S gradient layers. *J. Mar. Res.* **56**, 157–196.

Stern, M. E. & Turner, J. S. 1969 Salt fingers and convective layers. *Deep-Sea Res.* **16**, 497–511.

Taylor, J. R. 1993 Anisotropy of salt fingers. *J. Phys. Oceanogr.* **23**, 554–565.

Taylor, J. R. & Veronis, G. 1996 Experiments on doubly-diffusive sugar-salt fingers at high stability ratio. *J. Fluid Mech.* **321**, 315–333.

Turner, J. S. 1967 Salt fingers across a density interface. *Deep-Sea Res.* **14**, 499–611.

https://doi.org/10.1017/S0022112000002135 Published online by Cambridge University Press